Numerical Study on the Interaction Characteristics between Attached Cavitation and Velocity Boundary Layer under Different Working Conditions

Q. Ma[1,2,3,4], F. Gu[2†] and L. Ji[2]

¹ School of Mechanical and Electrical Engineering, Chuzhou University, Chuzhou 239000, China
² National Research Center of Pumps, Jiangsu University, Zhenjiang 212013, China
³ School of Mechanical Engineering, Hefei University of Technology, Hefei 230009, China
⁴ Anhui Liuxiang Special Ship Co., Ltd., Mingguang 239400, China

†Corresponding Author Email: 2211911004@stmail.ujs.edu.cn

ABSTRACT

Attached cavitation often occurs on the blade surface of hydraulic machinery, negatively affecting its performance. The SST k-ω turbulence model and SS cavitation model are employed to calculate the attached cavitation on the surface of the NACA0015 hydrofoil to explore the interaction between attached cavitation and the velocity boundary layer. The findings are systematically analyzed from four aspects: flow field characteristics, vortex dynamics, boundary layer characteristics, and energy loss. The results indicated that the spanwise effect of the surface flow field of the hydrofoil is more pronounced at low cavitation numbers. From the perspective of vortex dynamics, each vortex transport term is sensitive to the change in cavitation number, and the trend of each vortex transport term varies with the change in cavitation number. The inverse pressure gradient region of the velocity boundary layer is primarily distributed in the tail of the attached cavity, significantly affecting the formation of the phase interface at the tail of the cavity and the cavity shedding. The energy loss on the suction surface of the hydrofoil is mainly concentrated in the velocity boundary layer, with PL1 and PL3 being the primary ones. When the interface of the attached cavity phase overlaps with the velocity boundary layer, it promotes the energy loss of the local fluid. When the attached cavity completely covers the velocity boundary layer, the energy loss in the boundary layer is significantly reduced.

1. INTRODUCTION

In hydraulic machinery, when the internal liquid's local pressure drops below the liquid's saturated vapor pressure, a phase transition occurs within the liquid or near the solid-liquid interface, forming steam or gas cavities. This phenomenon is called cavitation (Ji et al., 2019; Gu et al., 2021). The generation of cavitation often affects the stable operation of the unit and, in severe cases, leads to a significant decline in the performance of hydraulic machinery (Yi, 2017; Gu et al., 2024), significantly shortening its service life (Arndt, 1981; Franc & Michel, 2006; Kumar & Saini, 2010; Luo et al., 2016). Attached cavitation, a prevalent type in hydraulic machinery, often forms on the back of blades. As cavitation lengthens, slice cavitation gradually develops into unstable cloud cavitation. During the relatively stable stage of blade cavitation, the cavitation changes the blade load

distribution and deviates from the rated operating condition. Simultaneously, high-frequency, small-scale cavitation detaches at the tail of the cavitation zone, intensifying noise and vibration (Kjeldsen et al., 2000; Kawanami et al., 2002; Zhang et al., 2015; Wang et al., 2014). Since blade cavitation typically adheres to the back of the blade, it interacts with the velocity boundary layer on the blade surface, affecting the mechanical properties, operational stability, and service life of the blade. Therefore, a comprehensive understanding of the relationship between attached cavitation and the boundary layer is crucial for the safe operation of hydraulic machinery.

Hydraulic mechanical blades can often be viewed as stacked sections of hydrofoils. To avoid the interference of numerous factors, such as blade rotation and tip leakage vortex (Brennen, 2013), relevant research on blade attachment cavitation is often based on hydrofoils. On this

NOMENCLATURE			
ρ	density	σ	cavitation number
u	velocity	m_e	source term of vaporization
t	time	m_c	source term of condensation
p	pressure	b	width of the hydrofoil
μ	dynamic viscosity	c	chord length of the hydrofoil
k	turbulent kinetic energy	p_c	pressure coefficient
Re	Reynolds number	A^*	distribution of dimensionless area of bubbles
α	angle of attack	P^*	dimensionless pressure distribution
p_v	saturated vapor pressure	ω	vorticity
v_t	vortex viscosity	P_L	power loss
α_v	volume fraction of the gas phase		

basis, if only a single hydrofoil is selected as the research object, the effect factors of leaf and sand can be removed (Tsujimoto et al., 2009; Iga et al., 2011). Although attached cavitation on stationary isolated hydrofoils differs from that on three-dimensional twisted rotating blades, it is challenging to investigate three-dimensional twisted blades directly. Hence, it can only be improved gradually from simple to complex. Practice proves that the cavitation mechanism obtained on the stationary hydrofoil is also of great guiding significance for the rotating blade (Brennen, 2011, 2013).

Existing research indicates that even with low nucleation content in the inflow, attached cavitation will still occur, albeit with a different morphology. At this stage, cavitation does not occur at the leading edge of the void and is commonly referred to as flow-induced attached cavitation (Leger & Ceccio, 1998). One primary issue explored in this paper is boundary layer separation. When fluid flows over a hydrofoil surface, viscous effects create a reverse pressure gradient near the wall. Flow separation, also known as boundary layer separation, occurs if the fluid's kinetic energy is insufficient to counter this reverse pressure gradient. This phenomenon can readily lead to hydrofoil stall, a critical issue in fluid dynamics. Flow separation on hydrofoils includes several forms, such as laminar separation, laminar separation bubbles, and turbulent separation. The location of separation extends from the trailing edge to the leading edge of the hydrofoil, with the form and position of separation closely related to the operating conditions, such as angle of attack and flow velocity (Schlichting & Gersten, 2016). The velocity boundary layer on the hydrofoil's surface significantly impacts the formation of attached cavitation (Arakeri, 1975). When separation bubbles occur in the boundary layer, significant fluctuations arise in the fluid, which reattaches to the wall after laminar separation. This leads to the initial formation of nuclei, creating tiny bubbles at that location. Subsequently, these bubbles develop and expand within the boundary layer, extending upstream until the leading edge of the bubble reaches a new equilibrium position. Therefore, studying boundary layer separation not only enhances understanding of the aerodynamic performance of hydrofoils but also reveals how attached cavitation on the hydrofoil's surface alters the characteristics of boundary layer separation, increasing the complexity of the hydrofoil's mechanical performance. Current research on attached cavitation in hydrofoils primarily focuses on the periodic shedding process of cloud cavitation that occurs as the attached

cavitation intensifies, known as partial cavity oscillation (PCO). Under PCO conditions, cavitation occurs periodically on the suction side of the hydrofoil, forming and shedding, then collapsing near the blade. This leads to direct blade damage, causing severe vibrations and noise, among the most detrimental states of cavitation in hydraulic machinery (Kawanami et al., 1998). The current research on PCO primarily focuses on two aspects: the re-entrant jet and shock waves.

Long et al. (2018), Dang & Kuiper (1999), and Laberteaux & Ceccio (2001) examined the effect of the re-entrant jet on three-dimensional hydrofoils, observing that the cross-section of the hydrofoils progressively changes along the spanwise direction. The cavities' length increases along the span, and the cavitation closure line inclines relative to the flow direction. The direction of the re-entrant jets formed in the cavitation closure area is approximately perpendicular to the closure line. Foeth et al. (2008) explored the characteristics of cavitation formation and shedding and the development patterns of re-entrant jets on three-dimensional twisted hydrofoils. Arndt et al. (2000) noted a transient disappearance phenomenon at the leading edge of cavities, indicating that it can be attributable to the action of a shock wave. Schneer et al. (2008) documented the shock waves generated by the collapse of cavities through simulations and examined their effects on attached cavitation. In 2015, Professor Ceccio's team utilized X-ray technology to measure the transient gas content distribution within cavities in a Venturi section, thus confirming the presence and action of shock waves (Ganesh et al., 2016). Ganesh (2015) determined that such shock waves are not impeded by surface obstacles during transmission. Budich et al. (2018) applied the Large Eddy Simulation method to model experiments conducted by Ceccio and colleagues, achieving a high degree of agreement between the simulation outcomes and the experimental data.

Accordingly, although significant research achievements have been made in the field of attached cavitation, studies exploring the interaction between attached cavitation and boundary layer separation remain scarce. For example, the influence of attached cavitation on boundary layer separation before and after its occurrence is still unclear. Additional research is necessary to determine the effects of boundary layer separation on attached cavitation. Hence, this study concentrates on the extensively studied single three-dimensional NACA0015 hydrofoil, which boasts a wealth

of experimental and simulation data, to examine the distribution characteristics of attached cavitation along the span of the hydrofoil (Kawakami et al., 2008; Wan, 2019). The vortical dynamics characteristics of attached cavitation are analyzed using the vorticity transport equation. The research assesses the effects of various cavitation conditions on the boundary layer. It introduces an energy balance equation derived directly from the Navier-Stokes (N-S) equations to explore the energy distribution characteristics within the boundary layer of attached cavitation. The objective is to indicate the interactions and energy loss characteristics between attached cavitation in its relatively stable sheet cavitation stage and the velocity boundary layer on the hydrofoil surface. This analysis should provide a reference for the management of attached cavitation.

2. METHODOLOGY

2.1 Governing Equations

This study uses a homogeneous equilibrium flow model to simulate gas-liquid two-phase cavitation flow. The model considers the density of the gas-liquid mixture as a consistent single density, with identical flow rates and pressures across the mixture. The fundamental governing equations include the continuity equation and the momentum equation.

1. Continuity Equation.

The fluid flow process follows the law of conservation of mass, governed by the continuity equation.

$$\frac{\partial \rho_m}{\partial t} + \frac{\partial}{\partial x_j}\left(\rho_m u_j\right) = 0 \tag{1}$$

where $\rho_m = \rho_l(1-\alpha_v)+\rho_v\alpha_v$ is the density of gas-liquid mixed medium, kg/m^3; t is time, s; u_j (j = 1, 2, 3) is the component of the velocity $\vec{u}$ in the j direction, m/s; α_v is the gas phase volume fraction.

2. Momentum Equation.

Similarly, the process follows the law of conservation of momentum, which is governed by the momentum equation.

$$\frac{\partial}{\partial t}\left(\rho_m u_i\right) + \frac{\partial}{\partial x_j}\left(\rho_m u_i u_j\right) = -\frac{\partial p}{\partial x_i} +$$
$$\frac{\partial}{\partial x_j}[(\mu_m + \mu_t)\left(\frac{\partial u_i}{\partial x_j} + \frac{\partial u_j}{\partial x_i} - \frac{2}{3}\frac{\partial u_k}{\partial x_k}\delta_{ij}\right)] \tag{2}$$

where $u_{i/j/k}$ (i, j, k = 1, 2, 3) is the velocity component, m/s; $x_{i/j}$ (i, j = 1, 2, 3) is the position, m; t is time, s; p is pressure, Pa; $\mu_m = \mu_l(1-\alpha_v) + \mu_v\alpha_v$ is laminar dynamic viscosity of gas-liquid mixed medium, Pa·s; μ_t is the turbulent dynamic viscosity, Pa·s. This parameter is often solved using various turbulence models; δ_{ij} is the symbol of the Kronecker function: when $i = j$, $\delta_{ij} = 1$, when $i \neq j$, $\delta_{ij} = 0$.

2.2 Turbulence Models

The SST k-ω model combines the k-ω model and k-ε model. The k-ω model addresses the low Reynolds

number issues near the wall, while the k-ε model simulates these issues at the far wall. The SST k-ω encompasses equations for turbulent kinetic energy k, turbulent frequency ω, and eddy viscosity v_t.

The following is the turbulent kinetic energy k equation:

$$\frac{\partial(\rho k)}{\partial t} + \frac{\partial(\rho k u_i)}{\partial x_j} = \frac{\partial}{\partial x_j}[\mu_m + \frac{\mu_t}{\sigma_k}\frac{\partial k}{\partial x_j}]$$
$$+ P_k - \beta' \rho k\omega \tag{3}$$

The turbulent frequency ω equation is as follows:

$$\frac{\partial(\rho\omega)}{\partial t} + \frac{\partial(\rho\omega u_i)}{\partial x_j} = \frac{\partial}{\partial x_j}[(\mu_m + \frac{\mu_t}{\sigma_\varepsilon})\frac{\partial\omega}{\partial x_j}] +$$
$$\alpha\frac{\omega}{k}P_k - \beta\rho\omega^2 + 2(1-F_1)\rho\frac{1}{\sigma_{\omega 2}\omega}\frac{\partial k}{\partial x_j}\frac{\partial\omega}{\partial x_j} \tag{4}$$

The vortex viscosity v_t equation is as follows:

$$v_t = \frac{\alpha_1 k}{\max(\alpha_1, \omega, SF_2)} = \frac{\mu_t}{\rho} \tag{5}$$

where P_k is turbulence generation rate; S is a fixed estimate of the strain rate; The constants $\sigma_k = 2$, $\beta' = 0.09$, $\sigma_\omega = 2$, $\alpha = 5/9$, $\beta = 0.075$, $\sigma_{\omega 2} = 1/0.856$.

Mixed function F_1 equation:

$$F_1 = \tanh(\text{arg}_1^4) \tag{6}$$

The following is a mixed function F_2 equation:

$$F_2 = \tanh(\text{arg}_2^2) \tag{7}$$

where

$$\text{arg}_1 = \min(\max(\frac{\sqrt{k}}{\beta\omega y}, \frac{500v}{y^2\omega}), \frac{4\rho k}{CD_{KW}\sigma_{\omega 2}y^2}) \tag{8}$$

$$\text{arg}_2 = \max(\frac{2\sqrt{k}}{\beta'\omega y}, \frac{500v}{y^2\omega}) \tag{9}$$

where

$$CD_{KW} = \max(2\rho\frac{1}{\sigma_{\omega 2}\omega}\nabla k\nabla\omega, 1.0\times10^{-10}) \tag{10}$$

where v is kinematic viscosity; y is the distance to the nearest wall.

2.3 Cavitation Models

Cavitation can be modeled using the following mass-transfer equation:

$$\frac{\partial\rho_v\alpha_v}{\partial t} + \frac{\partial(\rho_v\alpha_v u_j)}{\partial x_j} = m_e - m_c \tag{11}$$

where m_e and m_c are the source terms of vaporization and condensation, respectively. They have different descriptions in various cavitation models, such as the Schnerr-Sauer (SS) cavitation model (Sauer et al., 2000), as follows:
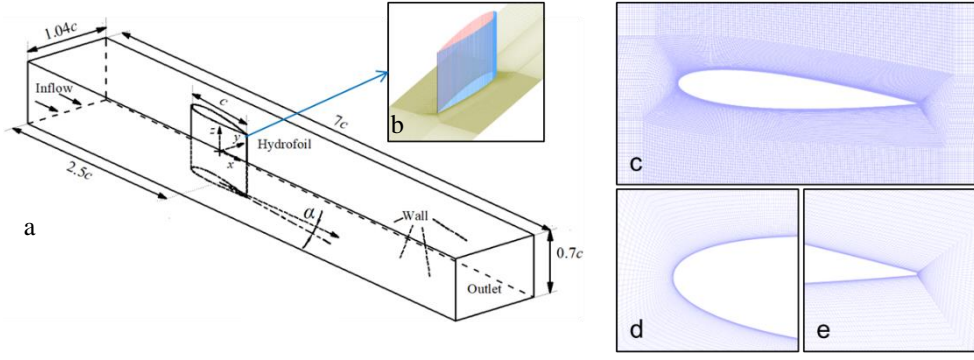
Fig. 1 Domain and Grids

Table 1 Flow field parameters

Inlet velocity, u_{in} (m/s)	Saturated vapor pressure, p_v (Pa)	Outlet pressure, p_{out} (Pa)	Cavitation number, σ	Reynolds number, *Re*
8	——	51025	Non-cavitation	918344
8	3540	35517	1.00	918344
8	3540	51025	1.49	918344
8	3540	67459	2.00	918344

$$\begin{cases} m_e = \dfrac{3\rho_v\rho_l}{\rho_m}\dfrac{\alpha_v(1-\alpha_v)}{R_B}\sqrt{\dfrac{2|p_v-p|}{3\rho_l}}\left(p \le p_v\right) \\ \\ m_c = \dfrac{3\rho_v\rho_l}{\rho_m}\dfrac{\alpha_v(1-\alpha_v)}{R_B}\sqrt{\dfrac{2|p-p_v|}{3\rho_l}}\left(p \ge p_v\right) \end{cases} \tag{12}$$

The SS model is derived based on bubble dynamics, incorporating the radius of the nucleus. The equation relates the nucleus radius R_B, the volume fraction of the gas phase α_v, and the number density of the nucleus n is $R_B = ((\alpha_v/(1-\alpha_v)(3/4\pi n))^{1/3}$, where n is an empirical constant, typically $n = 1 \times 10^{13}$.

2.4 Numerical Setup

Cervone et al. (2006) conducted cavitation experiments on a NACA0015 hydrofoil at the CPRTF laboratory. The results, published in ASME, have been internationally recognized for their significant experimental value. This research relies on the experimental model from the GPRTF laboratory, considering the entire development and stability of the flow (Kubota et al., 2006). The inlet was extended to twice the chord length of the hydrofoil, while the outlet was extended to four times the chord length. Figure 1a illustrates the computation domain creation. The hydrofoil has a chord length of c = 115 mm, a width of b = 0.7c, a height of 1.04c, and an angle of attack of α = 5°.

ICEM CFD software is utilized in this study to divide the NACA0015 hydrofoil into hexahedral structured meshes. The surface meshes are depicted in Figs. 1b and 1c. To enhance the mesh quality of the hydrofoil, a C-shaped structural mesh divides the leading edge, and the meshes at both the leading and trailing edges are locally encrypted, as illustrated in Figs 1d and 1e. The configuration of boundary conditions corresponds to the experimental setup. The inlet is designated as a velocity inlet, the outlet as a pressure outlet, and the wall implements a no-slip boundary condition. The residual value for convergence accuracy is set to 10^{-6}. The difference scheme adopts a high-order upwind scheme. The fluid medium comprises water and vapor, in which the density of water is 998.2 kg/m³, the dynamic viscosity is 0.001 Pa·s, and the saturated vapor pressure is 3540 Pa. Detailed boundary condition parameters of each operational condition are listed in Table 1, where the cavitation number σ is defined as follows:

$$\sigma = \frac{p_{out} - p_v}{0.5\rho_l u_{in}^2} \tag{13}$$

where P_{out} is the outlet pressure; p_v is the saturated vapor pressure; u_{in} is the inlet velocity. The Reynolds number *Re* is calculated using the following formula:

$$Re = \frac{\rho u_{in} c}{\mu} \tag{14}$$

The flow field around the NACA0015 hydrofoil is numerically determined at 25 °C using water under steady and non-cavitation conditions with three sets of grids of varying refinement degrees to verify the grid independence. The dimensionless pressure coefficient, p_c, is defined for comparison and validation against the experimental results (Cervone et al. 2006):

$$p_c = \frac{p - p_{out}}{0.5\rho_l u_{in}^2} \tag{15}$$

where p_{out} is the pressure outlet; u_{in} is the velocity inlet.

The calculation results are shown in Fig. 2a. The number of cells in the three groups is 1.14 million, 2.85 million, and 4.56 million, respectively. *Lc* is the percentage of the chord length of the hydrofoil. The results indicate that the reciprocal of the simulated pressure coefficients aligns well with the experimental values (Cervone et al., 2006). Mesh2 is selected for this study based on grid practicability, computational cost, y^+ values, and the criteria for verifying grid independence.
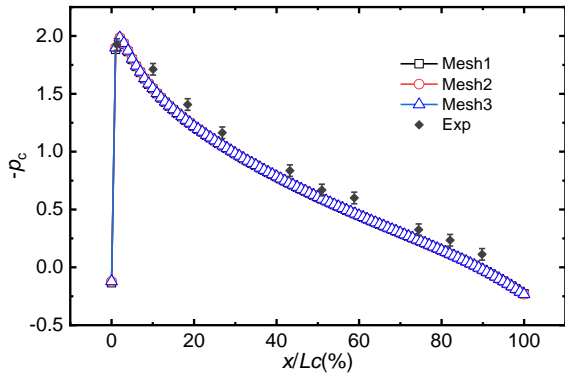
(a) Grid independence verification
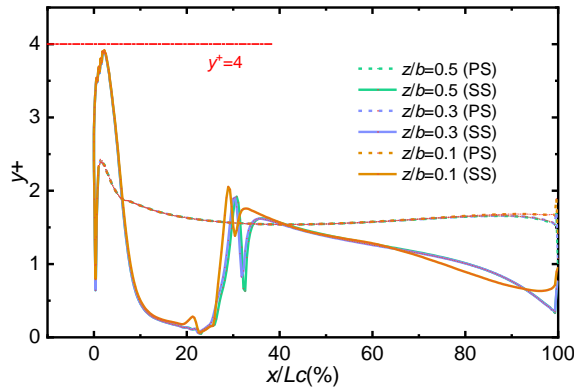
(b) *y+* value distribution of hydrofoil

Fig. 2 Grid verification

The quality of the boundary layer mesh on the hydrofoil significantly influences the accuracy of numerical calculations. The *y+* value is often employed to detect whether the mesh quality meets the accuracy requirements of the calculations. The distribution of *y+* values has no definite range, and the calculation requirements of *y+* values are different for various turbulence models. The range of *y+* values deemed acceptable by most scholars does not exceed 60, and results within this range exhibit high accuracy, closely matching the experimental data (Anderson & Benson, 1983; Matthew et al., 2004). Determining the *y+* value is an experimental process, necessitating calculations to adjust the height of the first layer of mesh near the wall until it fulfills the accuracy requirements. The finalized distribution of *y+* values on the hydrofoil's pressure and suction surfaces is shown in Fig. 2b, where the maximum *y+* value on the hydrofoil surface remains below 4.

3. VALIDATION

The SST *k-ω* turbulence model was utilized to conduct numerical simulations of cavitation in the flow field around the NACA0015 hydrofoil, resulting in the inverse pressure coefficient distribution on the hydrofoil's suction surface, as depicted in Fig. 3. The findings align with experimental results. On the suction surface of the hydrofoil within the attached cavity area, the inverse pressure coefficient derived from numerical calculations is slightly higher than the experimental data, as illustrated
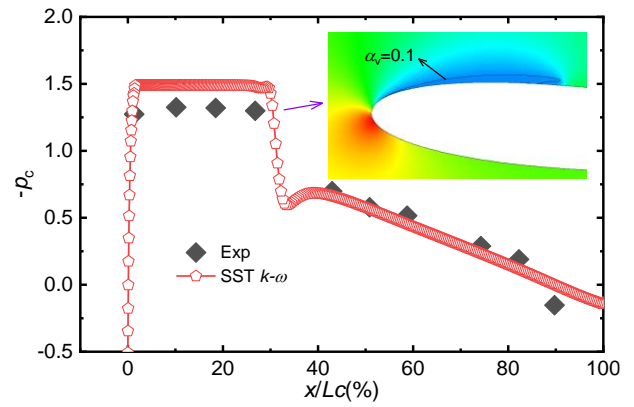

Fig. 3 Inverse distribution of pressure coefficient on the suction surface of hydrofoil

in Fig. 3. This discrepancy arises because the SS cavitation model does not account for the pressure inside the attached cavity. The model assumes that the pressure within the cavity equates to the saturated vapor pressure. Nevertheless, the simulation of cavitation morphology by current models adequately supports the research objectives of this study (Wan, 2019).

4. RESULTS AND DISCUSSIONS

4.1 The Spanwise Distribution Characteristics of Attached Cavitation

Figure 4(a) indicates that the pressure distribution, attached cavitation distribution, and flow field distribution on the surface of the hydrofoil at sections z/b = 0.1, 0.3, and 0.5 were extracted for different cavitation numbers to explore the spanwise distribution characteristics of hydrofoil attached cavitation. Figure 4(b) illustrates the pressure coefficient distribution on the hydrofoil's suction surface. The pressure distribution trend at various directional positions remains consistent under the same cavitation number. At σ = 2, no cavitation is present in the flow field, leading to a rapid drop in suction surface pressure from the leading edge's stagnation point to a peak at approximately x/Lc = 4, displaying a hump shape, followed by a gradual pressure increase. At σ = 1.49, the suction surface pressure decreases rapidly, and cavitation occurs at $-p_c$=1.5. Given that the cavitation model assumes the pressure inside the cavity equals the medium's saturated vapor pressure, the cavitation pressure coefficient appears nearly horizontal and linear. The pressure rises rapidly near the position x/Lc = 30, matching the absolute pressure drop rate at the leading edge. Then, the pressure fluctuates before rising slowly, similar to the pattern observed at σ = 2. At σ = 1, cavitation begins when the leading edge pressure of the hydrofoil rapidly drops to $-p_c$ = 1, followed by fluctuations around x/Lc = 86. Under conditions of low cavitation number, attached cavitation nearly covers the entire suction surface of the hydrofoil.

Figure 4(c) depicts the distribution of the dimensionless area of bubbles across each spanwise section under two cavitation conditions ($A^* = A_{cavity}/(bc)$). At σ = 1.49, the cavity area is consistent across each
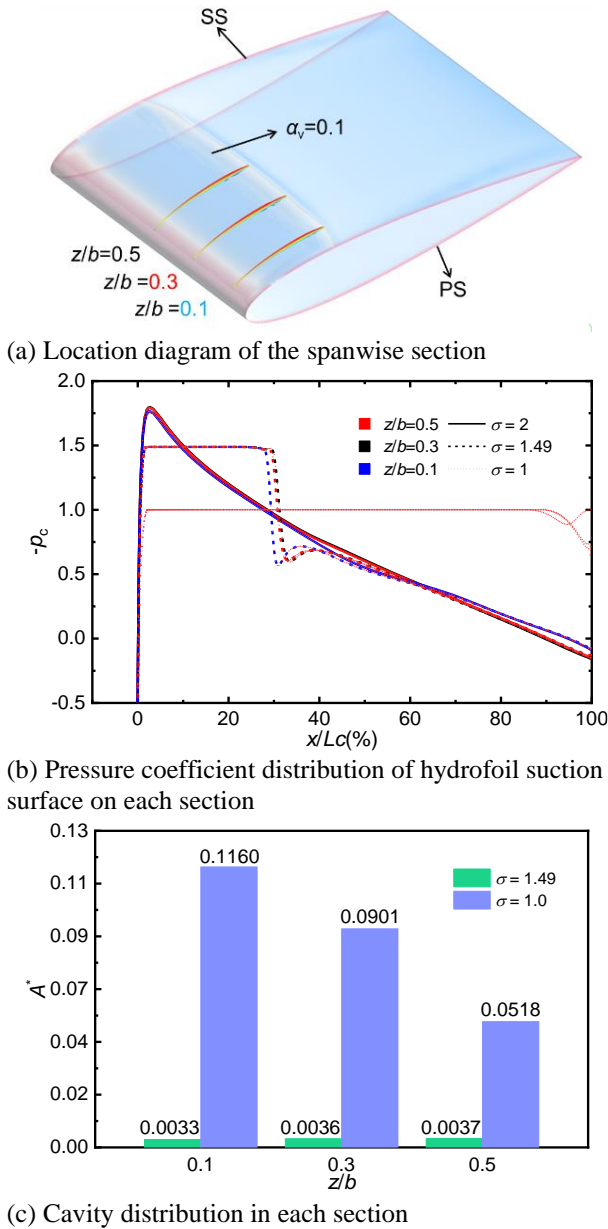
(a) Location diagram of the spanwise section

(b) Pressure coefficient distribution of hydrofoil suction surface on each section

(c) Cavity distribution in each section

Fig. 4 Spanwise distribution of attached cavitation

spanwise cross-section, with an average cavity area of approximately 0.0035. At $\sigma = 1$, the cavity area varies significantly across different spanwise cross-sections. The cavity areas at z/b=0.1, 0.3, and 0.5 are 0.1160, 0.0901, and 0.0518, respectively, averaging about 0.0860. This indicates that at low cavitation numbers, the cavity area of each section increases significantly and diminishes from the wall toward the middle of the hydrofoil span ($z/b = 0.5$) due to the wall surfaces' influence on both sides of the flow channel.

Figure 5 illustrates the dimensionless pressure distribution ($P^* = Pressure/P_v$), vorticity distribution ($\omega^* = \omega \cdot c/u_{in}$), cavity distribution ($\alpha_v = 0.1$), and velocity vector distribution of each section under cavitation conditions. The colors of the cavity contour lines distinguish different cross-sections. Generally, the pressure distribution of each transverse section of the hydrofoil is similar. The lower side, being the pressure surface, exhibits slightly higher pressure than the suction surface side above. The highest-pressure points in each section occur at the leading edge

stagnation point of the hydrofoil, whereas the low-pressure areas are near the leading edge of the suction side. With decreasing cavitation numbers, the flow field pressure generally lowers in each section while the vorticity on the hydrofoil's surface significantly increases. The vorticity separation point on the suction side of the hydrofoil surface is approximately $30\%c$ of the leading edge, and on the pressure side, it is located at the trailing edge's stagnation point. At $\sigma = 1.49$, the attached cavitation in each cross-section ranges from about 10% to $30\%c$ at the suction front edge. At $\sigma = 1$, the thickness and length of attached cavitation significantly increase, covering the entire suction surface of the hydrofoil. Velocity vector and local streamline distributions indicate the presence of local vortices at the tail of the attached cavitation, primarily caused by the boundary layer separation from the wall flow due to the inverse pressure gradient on the suction surface.

Accordingly, as the cavitation number decreases, the pressure in the flow field around the hydrofoil in each section significantly decreases, the vorticity on the hydrofoil's surface increases significantly, and the attached cavitation also substantially increases. Under identical operational conditions, the flow field distribution characteristics of each section are similar. Only under low cavitation conditions does the cavity area gradually decrease from the flow passage's sidewall to the hydrofoil span's middle section ($z/b = 0.1$ to z/b=0.5), influenced by tail cavity shedding and the flow channel wall effect.

4.2 Vortex Dynamics Characteristics of Attached Cavitation

The vorticity transport equation (VTE) (Wang et al., 2020) is utilized to explore the dynamic characteristics of vortices around hydrofoil-attached cavitation to investigate the interaction between attached cavitation and vortices, as described by the following equation:

$$\frac{D\boldsymbol{\omega}}{Dt} = (\boldsymbol{\omega}\cdot\nabla)\boldsymbol{V} - \boldsymbol{\omega}(\nabla\cdot\boldsymbol{V}) + \frac{\nabla\rho_m \times \nabla p}{\rho_m^2}$$
$$+ (\nu_m + \nu_t)\nabla^2\boldsymbol{\omega} \qquad (16)$$

where $D\boldsymbol{\omega}/Dt$ is the change rate of vorticity with time; $(\boldsymbol{\omega}\cdot\nabla)\boldsymbol{V}$ is the stretching and bending of vortices caused by changes in velocity; $\boldsymbol{\omega}(\nabla\cdot\boldsymbol{V})$ is the expansion and contraction of vorticity volume. The vortex baroclinic moment term $(\nabla\rho_m \times \nabla p)/\rho_m^2$ represents the shear moment caused by the non-parallelism of the iso-density surface, and the isobaric surface and $(\nu_m + \nu_t)\nabla^2\boldsymbol{\omega}$ represents the vortex viscosity diffusion caused by the fluid's viscosity. The effect of viscous diffusion on vorticity transport can be ignored since the minimum Reynolds number remains high in the studied condition. The terms within the vorticity transport equation are nondimensionalized for comparative analysis purposes. The terms on the right-hand side are represented by (*), and the calculation formula is as follows: $(*)^* = (*)\cdot c^2/ u_{in}^2$.

Figure 6 depicts the vorticity distribution at the $z/b = 0.5$ section under different cavitation numbers. It indicates that vorticity at this section is concentrated near the suction and pressure surfaces of the hydrofoil under various cavitation numbers. The vortex separation point
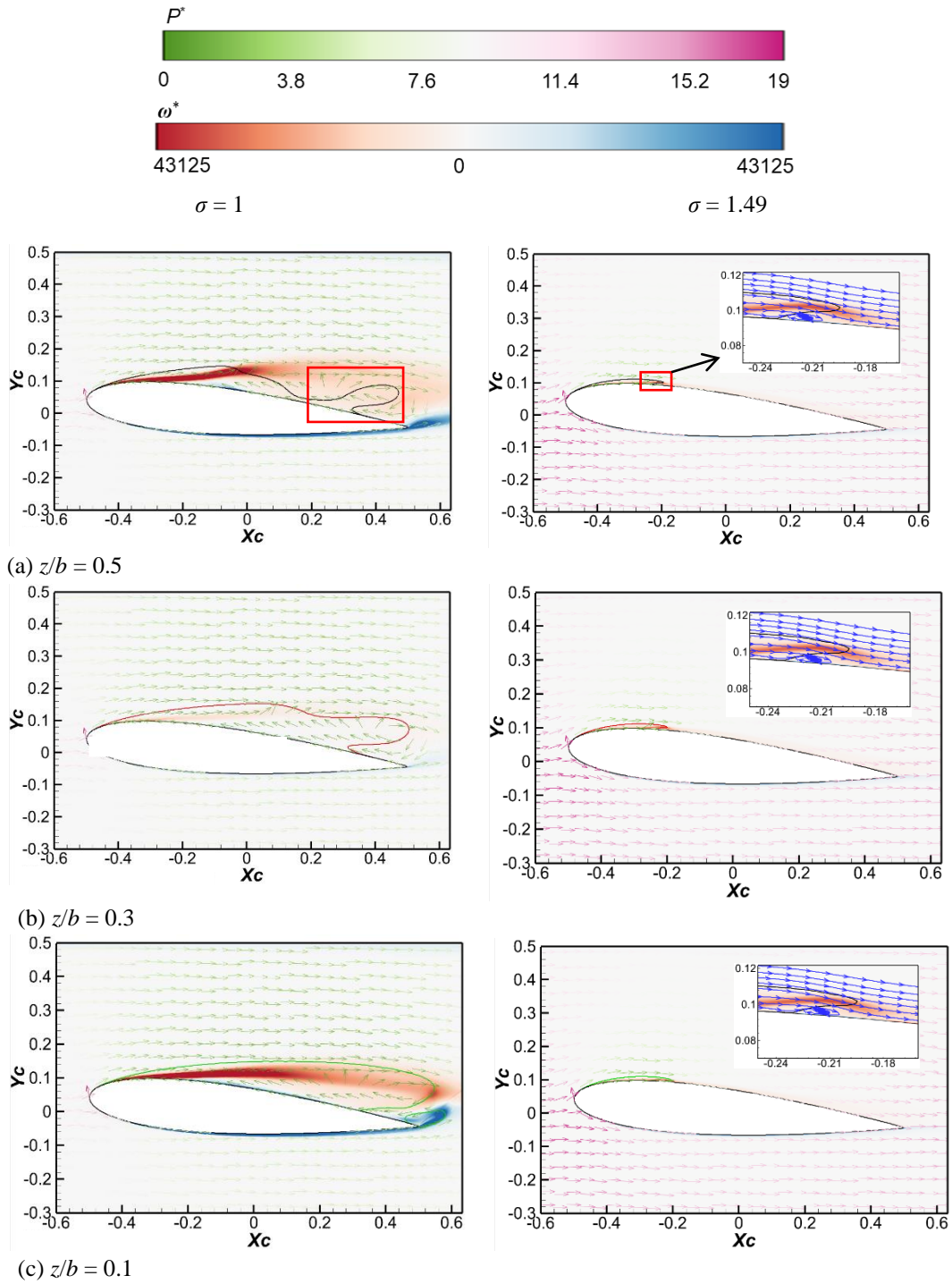
(a) *z/b* = 0.5

(b) *z/b* = 0.3

(c) *z/b* = 0.1

Fig. 5 Flow field distribution of each section
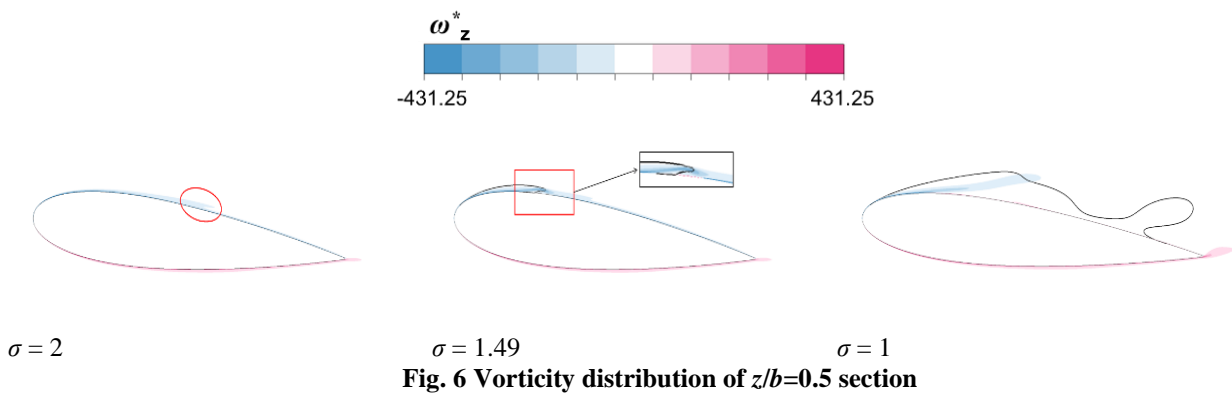
Fig. 6 Vorticity distribution of *z/b*=0.5 section

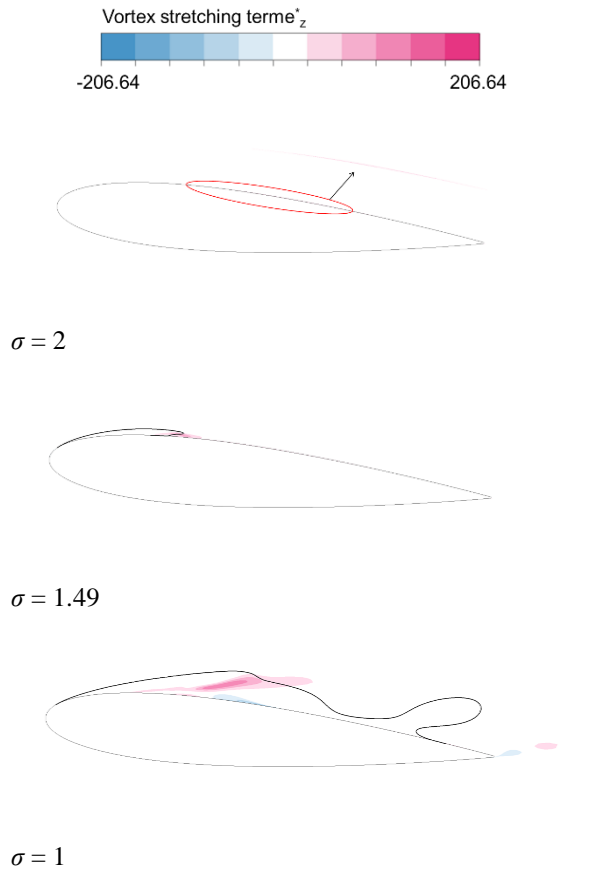**Fig. 7 Vortex tension term distribution of *z/b*=0.5 section**

Fig. 8 Baroclinic moment term distribution for *z/b*=0.5 section

on the suction surface is near the chord length's midpoint when $\sigma = 2$. As the cavitation number decreases, the vorticity separation point gradually moves toward the leading edge, a shift caused by the flow separation of the velocity boundary layer under the compression of the attached cavity. When $\sigma = 1.49$, the maximum suction vorticity is located at the phase interface of the trailing edge of the attached cavity. When $\sigma = 1$, the suction vorticity is primarily located inside the attached cavity, illustrating that attached cavitation significantly influences the vorticity distribution on the hydrofoil surface.

Figure 7 illustrates the vortex stretching term at the $z/b = 0.5$ section under different cavitation numbers. When $\sigma = 2$, only a small amount of vortex stretching occurs on the suction side of the hydrofoil. As the cavitation number reduces to $\sigma = 1.49$, the vortex stretching concentrates at the tail boundary of the attached cavity and the nearby suction surface. Although the overall shape of the attached cavity remains relatively stable, its tail phase interface is in a dynamic equilibrium under the impact of the return jet. When $\sigma = 1$, the vortex tension concentrates around $30\%c$ on the suction side of the hydrofoil and is primarily located within the cavity. This demonstrates that under low cavitation conditions, the spanwise stretching of the vortex inside the attached cavity becomes more obvious. In addition, the distribution law of the cavity area across different spanwise cross-sections also supports this observation.
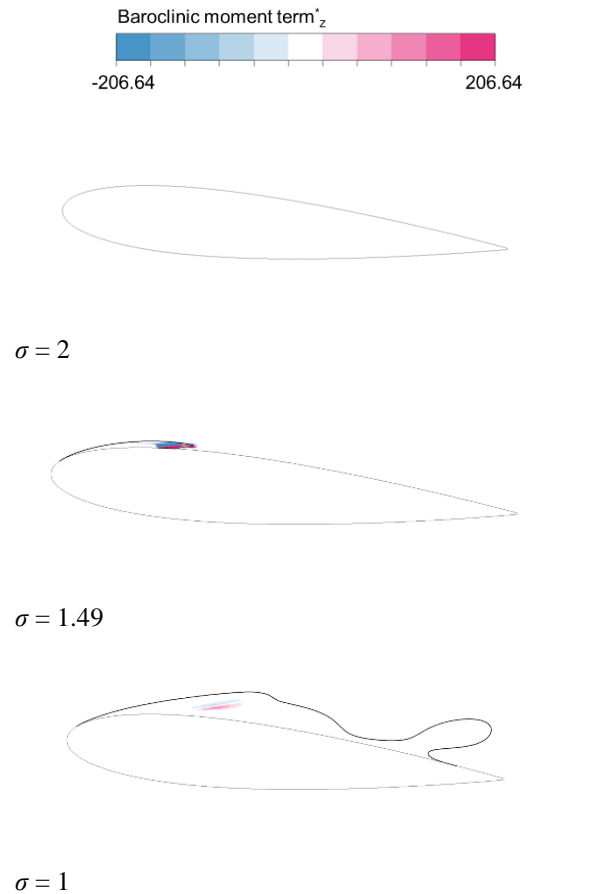
Figure 8 illustrates the distribution of the baroclinic moment term at the $z/b = 0.5$ section within the flow field under various cavitation numbers. The baroclinic moment term arises primarily due to the misalignment between the pressure gradient and the density gradient (Laberteaux & Ceccio, 2001). When $\sigma = 2$, the absence of cavitation in the flow field results in a zero-density gradient, eliminating the baroclinic moment term. At $\sigma = 1.49$, several factors contribute: firstly, the local density gradient alters with changes at the phase interface, where fluctuations frequently occur at the tail of the cavity. Secondly, this area is proximate to the velocity boundary layer on the suction surface, where significant pressure gradients exist. Finally, the distribution of local pressure gradients undergoes substantial changes under the compression from the attached cavity, concentrating the baroclinic moment term in this region. At $\sigma = 1$, the thickness and length of the attached cavity increase, covering the entire suction surface. The hydrofoil surface's velocity boundary layer is minimally affected by the density and pressure gradients near the phase interface, leading to only a small amount of the baroclinic moment term within the cavity. The baroclinic moment term contributes more significantly to vortex formation near the tail phase interface of the attached cavity as the cavitation number increases. However, its influence decreases with decreasing cavitation numbers.
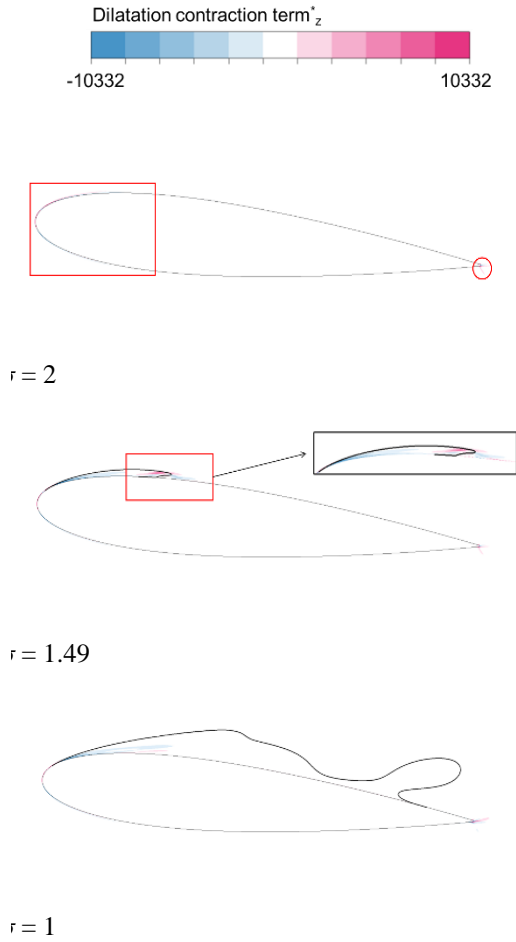
Fig. 9 Dilatation and contraction term distribution of *z/b*=0.5 section

Figure 9 shows the dilation and contraction terms at the *z/b* = 0.5 section across different cavitation numbers. At $\sigma = 2$, vortices primarily form near the stagnation points at the leading and trailing edges, concentrating the dilatation and contraction terms in these regions. These terms correlate with the rate of interphase mass transport, predominantly occurring in areas of cavity birth and collapse with obvious interphase mass transfer, such as the head and tail attached to the cavity (as shown in the operational condition when $\sigma = 1.49$). In contrast, at $\sigma = 1$, the dilatation and contraction terms are scant at the cavity's head since the attached cavity envelops the entire hydrofoil. In addition, since the morphology of the attached cavity is basically stable, the dilatation and contraction terms account for a relatively a minor proportion compared to other terms during vorticity transport.

4.3 Effect of Attached Cavitation on Boundary Layer

Velocities within the boundary layers along five lines parallel to the Y-axis (line1 to line5) were sequentially measured at positions *x/c* = 0.1, 0.3, 0.5, 0.7, and 0.9, aligned along the streamline on section *z/b*=0.5, as depicted in Fig. 10(a) to investigate the effect of attached cavitation on the boundary layer. Figure 10(b) to 10(f) shows the velocity boundary layers along line1 to line5 for three operational conditions, respectively. Comparatively,

the boundary layer velocities near the leading edge at line1 and line2 decrease due to the compression by the attached cavity. As the cavitation number lowers, this effect intensifies, and the velocity boundary layer thickens accordingly. The velocity boundary layer distribution in the non-cavity regions of the flow field, represented by line3 to line5, remains consistent under operational conditions at σ=2 and σ=1.49. When $\sigma = 1$, the attached cavity covers almost the entire suction surface, and the boundary layer's thickness increases obviously. At this time, the increase of the volume of the cavity has a squeezing effect on the fluid downstream of the cavity, so the mainstream flow rate of the downstream fluid increases slightly. In addition, the inverse pressure gradient region of the velocity boundary layer is primarily distributed within the tail of the attached cavity. It has an important effect on the formation of the phase interface at the tail of the cavity and the shedding of the cavity.

4.4 Power Loss Characteristics of Attached Cavitation

The energy balance equation in incompressible flow without temperature variation can be derived from the N-S equation and is presented as follows (Sun et al., 2022):

$$P_{\mathrm{L}} = -\int_{V} \frac{\partial\left(-\overline{u}_i\,\overline{\rho u_i'u_j'}\right)}{\partial x_j}dV + \int_{V} \mu \frac{\partial\left(-\overline{u}_i\,\overline{D}_{ij}\right)}{\partial x_j}dV$$
$$+\int_{V}\left(-\overline{\rho u_i'u_j'}\right)\frac{\partial \overline{u}_i}{\partial x_j}dV + \int_{V} \mu \overline{D}_{ij}\frac{\partial \overline{u}_i}{\partial x_j}dV \qquad (17)$$

where

$$D_{ij} = \frac{\partial u_i}{\partial x_j} + \frac{\partial u_j}{\partial x_i} \qquad (18)$$

$$-\overline{\rho u_i'u_j'} = \mu_{\mathrm{t}}\left(\frac{\partial \overline{u}_i}{\partial x_j} + \frac{\partial \overline{u}_j}{\partial x_i}\right) - \frac{2}{3}\delta_{ij}\rho k \qquad (19)$$

The energy loss is represented by four terms on the right side of Eq. (17), designated as PL_1 through PL_4. PL_1 denotes the diffusion of kinetic energy through Reynolds stress; PL_2 is the diffusion of kinetic energy using viscous stress; PL_3 is the production of turbulent kinetic energy due to the transformation of kinetic energy into turbulent kinetic energy; and PL_4 is the viscous dissipation of mean kinetic energy. The terms PL_1 and PL_2 possess both positive and negative values, indicating the direction of diffusion and energy exchange.

Figure 11 illustrates the cavitation profile and energy loss distribution in the flow field under various operating conditions. Figure 11 (a) indicates that when $\sigma = 2$, cavitation does not occur in the flow field, and the energy losses are primarily distributed on the surface of the hydrofoil. This distribution exhibits that the energy loss in the hydrofoil's flow field is related to the velocity boundary layer on the hydrofoil surface without cavitation. The analysis of the boundary layer velocity distribution on the hydrofoil's surface reveals a significant velocity gradient in this region, which induces substantial shear stress, enhancing viscous dissipation.
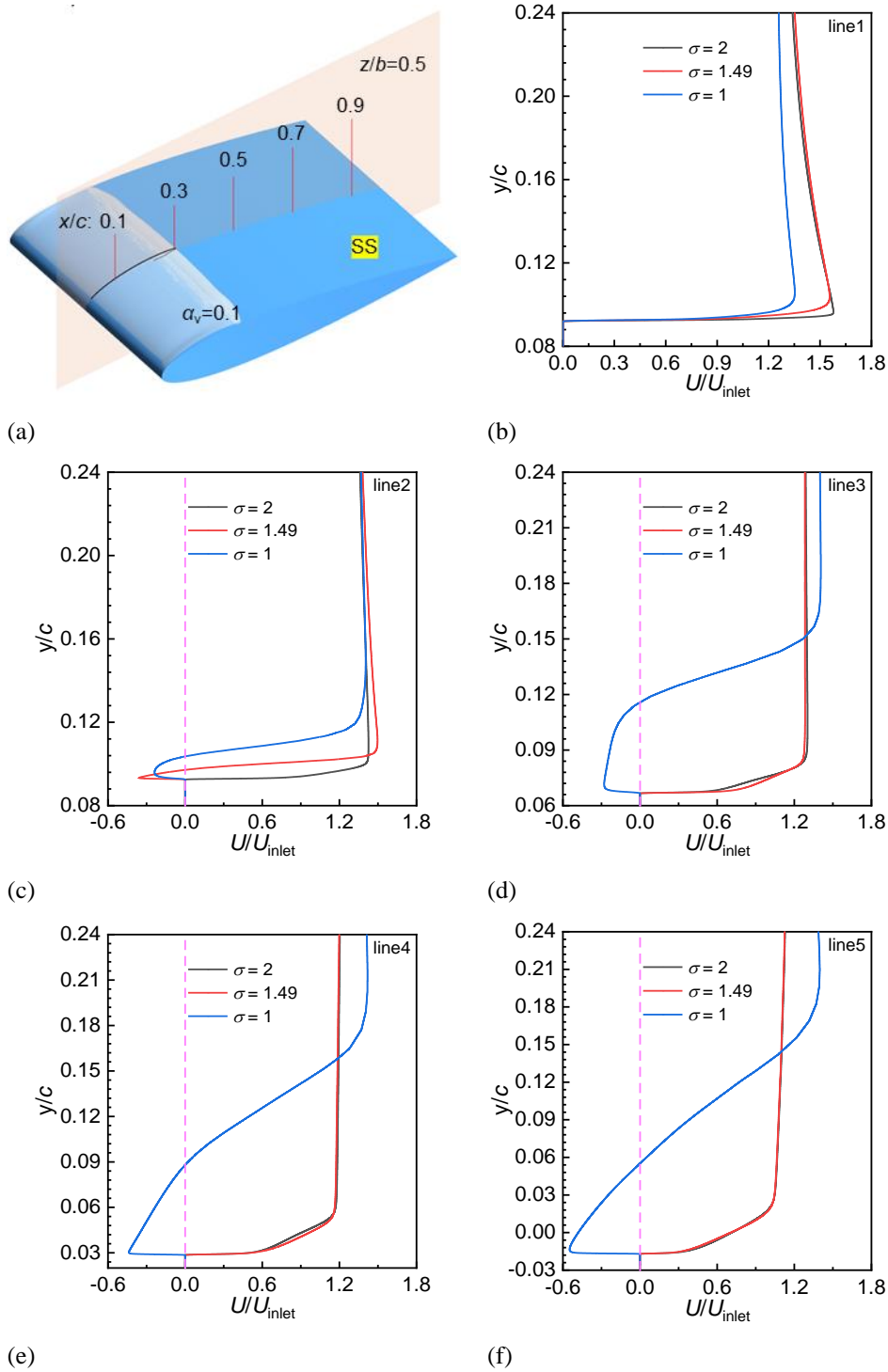
Fig. 10 Velocity boundary layer of hydrofoil suction surface (*z/b*=0.5)

Figure 11 (b) shows the distribution of each energy loss in the flow field when $\sigma = 1.49$. Compared to the condition $\sigma = 2$ (no cavitation), the generation of attached cavitation in the flow field exerts a more substantial influence on energy loss distribution. The energy loss on the pressure surface of the hydrofoil aligns with that observed under the condition $\sigma = 2$. However, on the suction surface, the attached cavity alters the distribution of each energy loss. Among these, PL_1 and PL_3 are primarily distributed near the phase interface attached to the tail of the cavity. Due to the separation of the velocity boundary layer and the shedding of the tail cavity, the

cavity interface at this position is consistently fluctuating, making the pressure at this position extremely unstable. Simultaneously, Fig. 5 shows that vortices exist here, significantly enhancing the local velocity gradient. This situation promotes the diffusion of kinetic energy through Reynolds stress and generates turbulent kinetic energy. For similar reasons, PL_2 is concentrated at the attached cavity's tail and distributed on both sides of the cavity interface. This distribution correlates with the compression of the fluid by the cavity, which compresses the fluid on the surface of the hydrofoil, resulting in the thickening of the velocity boundary layer. The cavity
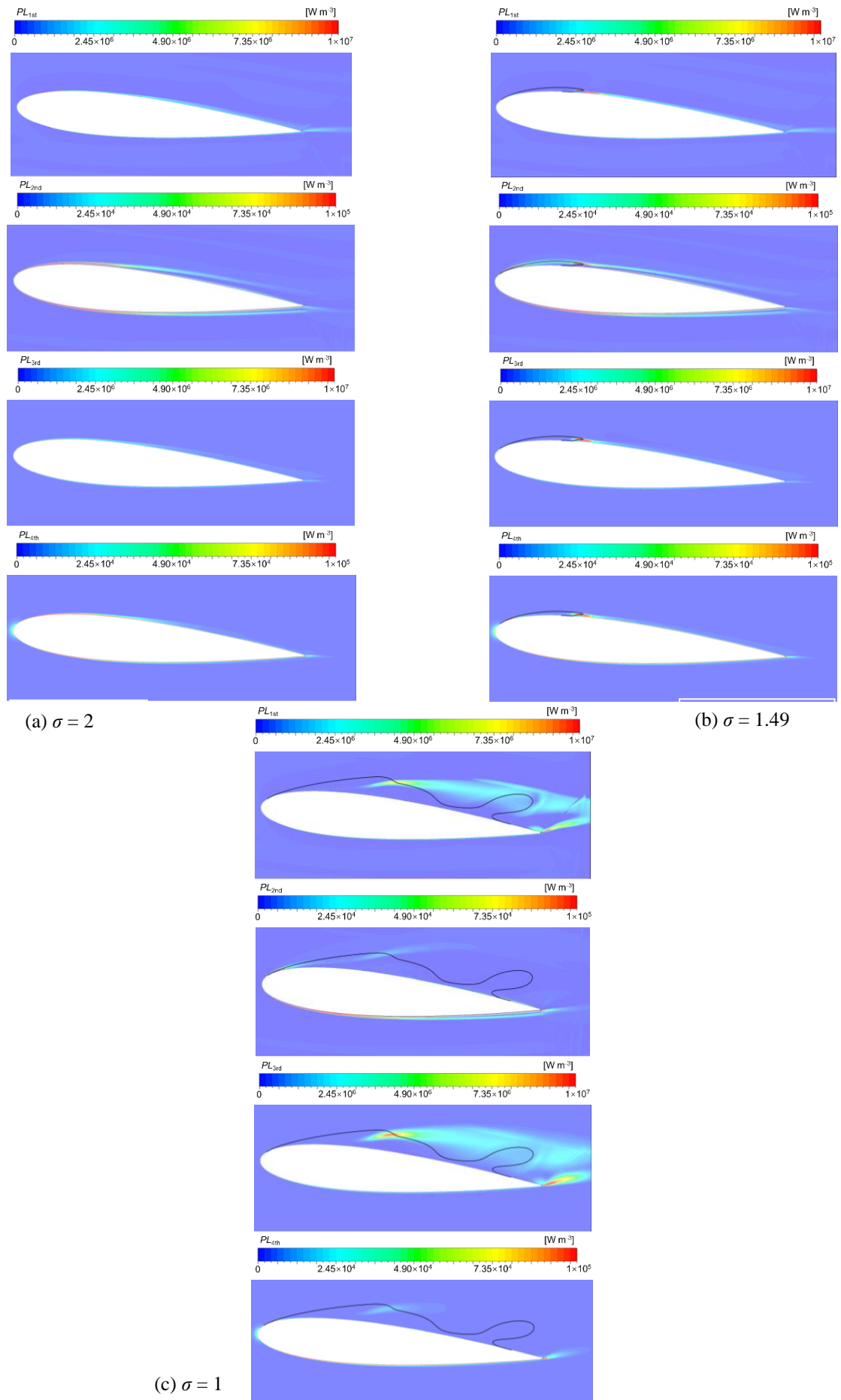
(a) $\sigma = 2$

(b) $\sigma = 1.49$

(c) $\sigma = 1$

Fig. 11 Distribution of cavity profile and energy loss in flow field under different working conditions (z/b=0.5)
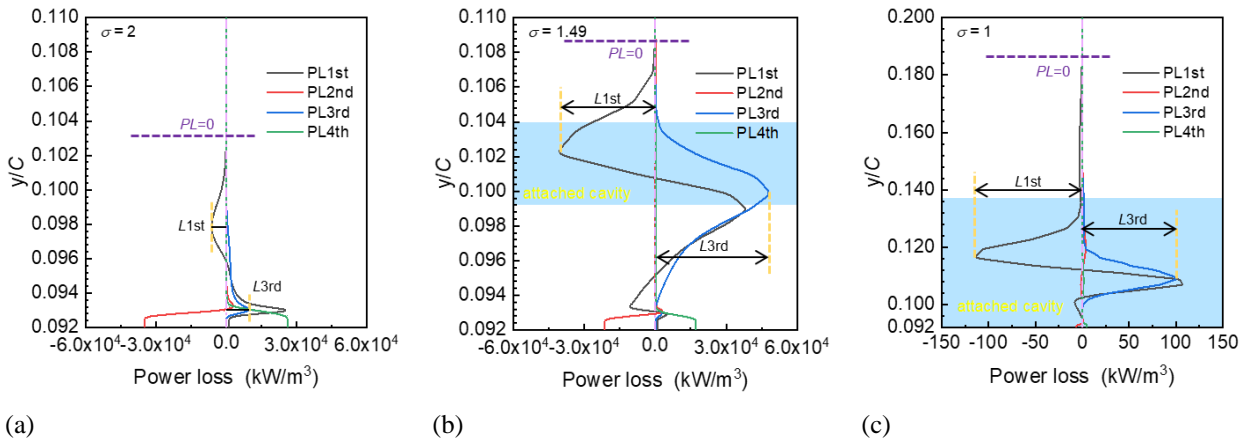
(a) (b) (c)

Fig. 12 Distribution of energy loss in the boundary layer of the stable phase interface of the cavity (line2) under different working conditions (z/b = 0.5)

interface within this thickened velocity boundary layer exhibits a huge velocity gradient, leading to substantial viscous shear stress in the flow field and thus facilitating the diffusion of kinetic energy through viscous stress. PL_4 is mainly distributed at the phase interface positions of the head and tail of the cavity. Combined with Fig. 4(b), it can be seen that the pressure gradient at the cavitation head and tail basins is enormous. As the fluid flows through these basins, the pressure drops abruptly to or from the saturated vapor pressure, causing significant changes in the average velocity of the fluid. When the fluid encounters the head of the hydrofoil, it initially strikes the leading edge and decelerates. It then enters the growth stage along the suction surface, corresponding to the sharp rise in the negative pressure coefficient of the surface. After the formation of the attached cavity on the surface of the front edge, the fluid in the basin is compressed, reducing the average flow velocity of the local fluid. Based on the cavitation model discussed in this study, the constant pressure inside the cavity equals the saturated vapor pressure. Hence, near the interface of the tail of the cavity, the medium transitions from the gas phase to the liquid phase along the flow direction, and the pressure increases sharply, leading to a decrease in the average flow velocity of the local fluid. Moreover, as mentioned earlier, vortices at this location also impede the upstream fluid, further diminishing the average flow velocity of the local fluid. Thus, the average kinetic energy of the fluid is depleted at these two locations.

Figure 11 (c) depicts the distribution of energy losses in the flow field when $\sigma = 1$. Compared with the condition $\sigma = 1.49$, the distribution of energy losses in the downflow field under this condition differs significantly from that under $\sigma = 1.49$. PL_1 and PL_3 are primarily distributed near the irregular phase interface of the cavitation tail and the trailing edge of the hydrofoil. The kinetic energy in the basin is mainly diffused by Reynolds stress and converted into turbulent kinetic energy. This diffusion indicates that the instability of attached cavity morphology is significantly enhanced at low cavitation numbers. It increases pressure and velocity fluctuation in the suction surface's downstream flow field, resulting in fluid flow loss. PL_2, on the suction side, is still distributed in the thickened velocity boundary layer for reasons consistent

with those described previously. PL_4, also on the suction side, is mainly distributed at the cavity's leading edge, the chord length's middle phase interface with sharp fluctuations, and the trailing edge of the hydrofoil. The causes of energy loss at the positions of the cavitation front and the hydrofoil tail are the same as those under the operational condition $\sigma = 1.49$. However, local viscous dissipation is also at the cavity phase interface near the middle chord length. Although the attached cavity covers almost the entire suction surface under the condition $\sigma = 1$, the phase interface near the middle of the chord length deforms significantly. This deformation indicates that the attached cavity before the distortion point of the phase interface is stable, with minimal phase interface fluctuation. The cavity morphology behind the distortion point is unstable and is undergoing significant changes. This instability arises because the cavity behind the distortion point is located in the wake region, where the velocity boundary layer is separated, and the region is characterized by extensive backflow and complex vortices, significantly influencing cavity formation. Hence, the flow field near the distortion point of the phase interface is slowed by the extrusion of the downstream return jet, resulting in local viscous dissipation of mean kinetic energy at this position.

In order to explore the energy exchange mechanism between the attached cavitation and the boundary layer, this study relies on previous analyses to extract various energy loss densities in the velocity boundary layer near the stable phase interface (line2) at the tail of the cavitation under different working conditions, as illustrated in Fig. 12. Fig. 12(a) displays the distribution of each energy loss density under the working condition where $\sigma = 2$ (no cavitation). At this point, all energy losses are concentrated in the boundary layer near the surface of the hydrofoil. The distribution range of PL1 is slightly wider, with a local loss of PL_1 occurring around $y/c = 0.098$, although its peak value is not half that observed in the boundary layer. Conversely, when cavitation occurs in the flow field ($\sigma = 1.49$), as depicted in Fig. 12(b), the densities of PL_1 and PL_3 significantly increase. Their peak positions rise under the influence of cavity extrusion but remain within the velocity boundary layer. As the cavitation number decreases from 2 to 1.49, the peak value

of PL_1 escalates by nearly six times ($L1st_{\sigma=1.49}/L1st_{\sigma=2\approx6}$), and the peak value of PL3 increases by nearly five times ($L3rd_{\sigma=1.49}/L3rd_{\sigma=2\approx6}$). This increase is likely because the location is near the interface of the tail phase of the attached cavity, which is situated within the velocity boundary layer under cavitation conditions. At this stage, the attached cavity directly compresses the fluid in the boundary layer, promoting the diffusion of kinetic energy through Reynolds stress and generating turbulent kinetic energy. Hence, the densities of PL_1 and PL_3 increase substantially. When the cavitation number further reduces to $\sigma = 1$, the site is enveloped by the attached cavity, and the boundary layer is completely encased within the cavity. Due to the constant pressure inside the cavity (saturated vapor pressure), the energy loss in the boundary layer is significantly reduced. Compared to the conditions of $\sigma = 2$ and $\sigma = 1.49$, the peak value of each energy loss density declines by two orders of magnitude. This reduction occurs because the complete coverage of the attached cavity thickens the velocity boundary layer, lowers the $\mathrm{d}u/\mathrm{d}y$ in this region, and decreases the shear stress, thus stabilizing the fluid and reducing the density of local fluid energy losses.

Accordingly, whether cavitation occurs or not, the energy loss at the suction surface of the hydrofoil is mainly concentrated within the velocity boundary layer, with PL_1 and PL_3 being the main types. When the phase interface of the cavity overlaps with the velocity boundary layer, it enhances the energy loss of the local fluid. In contrast, when the attached cavity fully envelops the velocity boundary layer, the energy loss within the boundary layer is significantly reduced. Hence, without considering the impacts of cavitation shedding and cavitation erosion on the mechanical properties of the hydrofoil, the cavitation conditions can be managed such that the attached cavitation fully covers the velocity boundary layer on the surface of the hydrofoil. This strategy aids in reducing the energy loss in the hydrofoil's velocity boundary layer and in enhancing the stability of the hydrofoil surface flow field.

5. CONCLUSION

The flow field of attached cavitation on the surface of the NACA0015 hydrofoil is numerically calculated using computational fluid dynamics. The study's conclusions can be drawn as follows:

(1) As the cavitation number decreases, the pressure around the hydrofoil in each spanwise section significantly drops. The vorticity on the hydrofoil surface increases and the volume of the attached cavity expands considerably. Under low cavitation conditions, the cavitation area diminishes from the flow passage sidewall to the middle section of the hydrofoil span ($z/b = 0.1 - z/b = 0.5$) due to tail cavity shedding and flow channel wall effects.

(2) With the decrease of the cavitation number, the vortex separation point gradually shifts toward the front edge, influenced by the boundary layer of compressed cavity velocity. Under low cavitation conditions, the vortex stretching within the attached cavity along the

spanwise direction becomes more obvious. At higher cavitation numbers, the baroclinic moment term plays a greater role in vortex formation near the tail phase interface. However, as the cavitation number decreases, its influence diminishes. The expansion and contraction terms, primarily focused on the cavity initiation and collapse sites with evident interphase mass transfer, constitute a relatively minor proportion compared to other terms.

(3) The velocity in the boundary layer decreases due to the compression by the attached cavity. This effect intensifies with the decrease of the cavitation number, and the velocity boundary layer gradually thickens. The inverse pressure gradient region within the velocity boundary layer is primarily located at the tail of the attached cavity and plays a crucial role in forming the phase interface at the cavity's tail and in the shedding of the cavity.

(4) The energy loss in the hydrofoil flow field correlates with the velocity boundary layer on the hydrofoil surface. Regardless of cavitation occurrence, the energy loss on the suction surface of the hydrofoil is primarily focused in the velocity boundary layer, with PL_1 and PL_3 as the main types. The attached cavitation in the flow field influences the distribution of various energy losses. When the phase interface of the attached cavitation overlaps with the velocity boundary layer of the hydrofoil suction surface, it promotes the local fluid's energy loss. When the attached cavity fully covers the velocity boundary layer, the energy loss within the boundary layer is substantially reduced.

This study provides insights that can aid in controlling blade surface attached cavitation in hydraulic machinery. However, the unsteady evolution of the interaction between attached cavitation and the boundary layer requires further investigation. In addition, the influence of this interaction on the noise generated by the hydrofoil warrants a more detailed study, given its significance for hydraulic machinery.

CONFLICT OF INTEREST

The authors declare that they have no conflict of interest.

AUTHORS CONTRIBUTION

Qijiang Ma: Conception and design of study, acquisition of data, analysis and/or interpretation of data, drafting the manuscript, revising the manuscript critically for important intellectual content; **Fadong Gu**: Conception and design of study, analysis and/or interpretation of data, drafting the manuscript, revising the manuscript critically for important intellectual content;

Leilei Ji: Numerical simulation calculations, data integration and processing.

REFERENCES

Anderson, B. H., & Benson, T. J. (1983). *Numerical solution to the glancing sidewall oblique shock wave/turbulent boundary layer interaction in three-dimension.* NASA Technical Memorandum, https://doi.org/10.2514/6.1983-136

Arakeri, V. H. (1975). Viscous effects on the position of cavitation separation from smooth bodies. *Journal of Fluid Mechanics, 68*(4), 779-799. https://doi.org/10.1017/S0022112075001231

Arndt, R. E. (1981). Cavitation in fluid machinery and hydraulic structures. *Annual Review of Fluid Mechanics, 13*(1), 273-326. https://doi.org/10.1146/annurev.fl.13.010181.001421

Arndt, R. E., Song, C., Kjeldsen, M., He, J., & Keller, A. (2000, September 17-22). *Instability of partial cavitation: a numerical/experimental approach.* [Twenty-Third Symposium on Naval Hydrodynamics]. 2000 Val de Reuil, France. National Academies Press.

Brennen, C. E. (2011). *Hydrodynamics of pumps.* London, England: Cambridge University Press.

Brennen, C. E. (2013). *Cavitation and bubble dynamics.* Cambridge, UK: Cambridge University Press.

Budich, B., Schmidt, S. J., & Adams, N. A. (2018). Numerical simulation and analysis of condensation shocks in cavitating flow. *Journal of Fluid Mechanics, 838*, 759-813. https://doi.org/10.1017/jfm.2017.882

Cervone, A., Bramanti, C., Rapposelli, E., & Agostino, L. D. (2006). Thermal cavitation experiments on a NACA 0015 hydrofoil. *Journal of Fluids Engineering, 128*(2), 953-956. https://doi.org/10.1115/1.2169808

Dang, J., & Kuiper, G. (1999). Re-entrant jet modeling of partial cavity flow on three-dimensional hydrofoils. *Journal of Fluids Engineering, 121*(4), 781-787. https://doi.org/10.1115/1.2823537

Foeth, E. J., Van Terwisga, T., & Van Doorne, C. (2008). On the collapse structure of an attached cavity on a three-dimensional hydrofoil. *Journal of Fluids Engineering, 130*(7), 071303. https://doi.org/10.1115/1.2928345

Franc, J. P., & Michel, J. M. (2006). *Fundamentals of cavitation.* Netherlands: Springer Netherlands. https://doi.org/10.1007/1-4020-2233-6

Ganesh, H. (2015). *Bubbly shock propagation as a cause of sheet to cloud transition of partial cavitation and stationary cavitation bubbles forming on a delta wing vortex.* (Doctoral dissertation).

Ganesh, H., Makiharju, S. A., & Ceccio, S. L. (2016). Bubbly shock propagation as a mechanism for sheet-to-cloud transition of partial cavities. *Journal of Fluid Mechanics, 802*, 37-78. https://doi.org/10.1017/jfm.2016.425

Gu, F. D., Huang, Y. D., & Zhang, D. S. (2021). Cavitation of multiscale vortices in circular cylinder wake at Re = 9500. *Journal of Marine Science and Engineering, 9*(12), 1366. https://doi.org/10.3390/jmse9121366

Gu, F. D., Shi, L., Shen, X., Zhang, D. S., & van Esch B. P. M. (2024). Research on the suppression mechanism of a tip leakage vortex over a hydrofoil with double-control-hole structure. *Ocean Engineering, 293,* 116610. https://doi.org/10.1016/j.oceaneng.2023.116610

Iga, Y., Hashizume, K., & Yoshida, Y. (2011). Numerical analysis of three types of cavitation surge in cascade. *Journal of Fluids Engineering, 133*(7), 071102. https://doi.org/10.1115/1.4003663

Ji, B., Cheng, H. Y., Huang, B., Luo, X. W., Peng, X. X., & Long, X. P. (2019). Research progresses and prospects of unsteady hydrodynamics characteristics for cavitation. *Advances in Mechanics, 49*(00), 428-479. https://doi.org/10.6052/1000-0992-17-012

Kawakami, D. T., Fuji, A., Tsujimoto, Y., & Arndt, R. E. A. (2008). An assessment of the influence of environmental factors on cavitation instabilities. *Journal of Fluids Engineering, 130*(3), 031303. https://doi.org/10.1115/1.2842146

Kawanami, Y., Kato, H., & Yamaguchi, H. (1998). *Three-dimensional characteristics of the cavities formed on a two-dimensional hydrofoil.* Proceedings of the Third International Symposium on Cavitation, Grenoble, France, Laboratoire des Ecoulements Géophysiques et Industriels.

Kawanami, Y., Kato, H., Yamaguchi, H., Maeda, M., & Nakasumi, S. (2002). Inner structure of cloud cavity on a foil section. *JSME International Journal Series B Fluids and Thermal Engineering, 5*(3), 655-661. https://doi.org/10.1299/jsmeb.45.655

Kjeldsen, M., Arndt, R. E., & Effertz, M. (2000). Spectral characteristics of sheet/cloud cavitation. *Journal of Fluids Engineering, 122*(3), 481-487. https://doi.org/10.1115/1.1287854

Kubota, A., Kato, H., & Yamaguchi, H. (2006). A new modelling of cavitating flows a numerical study of unsteady cavitation on a hydrofoil section. *Journal of Fluid Mechanics, 240*(240), 59--96. https://doi.org/10.1017/S002211209200003X

Kumar, P., & Saini, R. (2010). Study of cavitation in hydro turbines—A review. *Renewable and Sustainable Energy Reviews, 14*(1), 374-383. https://doi.org/10.1016/j.rser.2009.07.024

Laberteaux, K. R., & Ceccio, S. L. (2001). Partial cavity flows. Part 2. Cavities Forming on Test Objects with Spanwise Variation. *Fluid Mech, 431*, 43–63. https://doi.org/10.1017/S0022112000002937

Leger, A. T., & Ceccio, S. L. (1998). Examination of the flow near the leading edge of attached cavitation. Part

1. Detachment of two-dimensional and axisymmetric cavities. *Journal of Fluid Mechanics, 376*, 690. https://doi.org/10.1017/S0022112098002766

Long, X. P., Cheng, H. Y., Ji, B., Arndt, R. E. A., & Peng, X. X. (2018). Large eddy simulation and Euler–Lagrangian coupling investigation of the transient cavitating turbulent flow around a twisted hydrofoil. *International Journal of Multiphase Flow, 100*, 41-56. https://doi.org/10.1016/j.ijmultiphaseflow.2017.12.002

Luo, X. W., Ji, B., & Tsujimoto, Y. (2016). A review of cavitation in hydraulic machinery. *Journal of Hydrodynamics, Ser B, 28*(3), 335-358. https://doi.org/10.1016/S1001-6058(16)60638-8

Matthew, S. C., David, F. F., Hak-Kim C., & Raper, J. A. (2004). Effect of design on the performance of a dry powder inhaler using computational fluid dynamics. Part 1: Grid structure and mouthpiece length. *Journal of Pharmaceutical Sciences, 93*(11), 2863-2876. https://doi.org/10.1002/jps.20201

Sauer, J., Winkler, G., & Schnerr, G.H. (2000). Cavitation and condensation-common aspects of physical modeling and numerical approach. *Chemical Engineering and Technology, 23*(8), 663–666. https://doi.org/10.1002/1521-4125(200008)23:8<663::aid-ceat663>3.0.co;2-h

Schlichting, H., & Gersten, K. (2016). *Boundary-layer theory*. springer.

Sun, L. Y., Pan, Q., Zhang, D. S., Zhao, R. J., & van Esch, B. P. M. (2022). Numerical study of the energy loss in the bulb tubular pump system focusing on the off-design conditions based on combined energy analysis methods. *Energy, 258*(0), 124794.

https://doi.org/10.1016/j.energy.2022.124794

Tsujimoto. Y., Watanabe, S., & Horiguchi, H. (2009). Cavitation instabilities of hydrofoils and cascades. International *Journal of Fluid Machinery and Systems, 1*(1), 38-46. https://doi.org/10.5293/IJFMS.2008.1.1.038

Wan, F. L. (2019). *Optimization of cryogenic submerged pump with an inducer and experiment research of cavitation performance*. (Master's thesis) Jiangsu University.

Wang, C. C., Wang, G. Y., & Huang, B. (2020). Characteristics and dynamics of compressible cavitating flows with special emphasis on compressibility effects. *Journal of Multiphase Flow, 130* (0), 103357. https://doi.org/10.1016/j.ijmultiphaseflow.2020.103357.

Wang, S. J., Wang, Y. C., Dai, W. G., & Li, B. (2014). Numerical analysis for sheet cavitation noise characteristic of countra-rotating propeller. *Journal of Ship Mechanics, 18*(07), 778-785. https://doi.org/10.3969/j.issn.1007-7294.2014.07.006

Yi, Q. (2017). *Microstructure design of hydrofoil surface and its influence on cavitation flow field*. (Master's thesis) Dalian University of Technology.

Zhang, D. S., Shi, L., Shi, W. D., Zhao, R. J., Wang, H. Y., & van Esch, B. P. M. (2015). Numerical analysis of unsteady tip leakage vortex cavitation cloud and unstable suction-side-perpendicular cavitating vortices in an axial flow pump. *International Journal of Multiphase Flow, 77*, 244-259. https://doi.org/10.1016/j.ijmultiphaseflow.2015.09.006